nature physics

ARTICLES

PUBLISHED ONLINE: 21 AUGUST 2017 | DOI: 10.1038/NPHYS4225

Nonlinear flow response of soft hair beds

José Alvarado[1], Jean Comtet[1], Emmanuel de Langre[2] and A. E. Hosoi[1]*

We are 'hairy' on the inside: beds of passive fibres anchored to a surface and immersed in fluids are prevalent in many biological systems, including intestines, tongues, and blood vessels. These hairs are soft enough to deform in response to stresses from fluid flows. Yet fluid stresses are in turn affected by hair deformation, leading to a coupled elastoviscous problem that is poorly understood. Here we investigate a biomimetic model system of elastomer hair beds subject to shear-driven Stokes flows. We characterize this system with a theoretical model that accounts for the large-deformation flow response of hair beds. Hair bending results in a drag-reducing nonlinearity because the hair tip lowers towards the base, widening the gap through which fluid flows. When hairs are cantilevered at an angle subnormal to the surface, flow against the grain bends hairs away from the base, narrowing the gap. The flow response of angled hair beds is axially asymmetric and amounts to a rectification nonlinearity. We identify an elastoviscous parameter that controls nonlinear behaviour. Our study raises the hypothesis that biological hairy surfaces function to reduce fluid drag. Furthermore, angled hairs may be incorporated in the design of integrated microfluidic components, such as diodes and pumps.

Mechanics has become increasingly soft: research interest in largely deformable structures has increased over the past decades. Whereas stiff structures typically deform according to linear mechanical frameworks, global deformations of soft structures often incur geometrical nonlinearities, even while local strains remain small, in the range of linear response[1]. One driver of interest in deformable structures comes from the observation that deformability characterizes many biological systems[2]. Studying the nonlinear deformation of biological structures can supplant qualitative descriptions with quantitative physical models in a wide range of systems, such as embryo development[3] and microorganism locomotion[4]. Mimicking biological behaviour in the lab has furthermore led to novel engineering designs, such as soft robotic locomotion[5] and anisotropic surface adhesion[6].

One prominent example of soft structures in biology is beds of anchored, elastic fibres (or hairs), which are often immersed in fluids. Small ($\sim$1 to 100 μm) hairs coat many biological surfaces. Examples include brush-border microvilli[7], papillae of tongues[8], primary cilia of kidney cells[9,10], and hyaluronans of blood vessels' glycocalyx[11–13]. These hair beds are usually immersed in fluids, and sufficiently deformable to bend in response to fluid flow. Seminal work by Vogel on flexible tree leaves subject to aerodynamic forces described how fluid stresses induce reconfiguration, or nonlinear deformations that reduce drag forces[14]. This work has inspired a body of research into the reconfiguration of various plants[15–17] as well as idealized systems[18–26]. However, these studies have been performed at high Reynolds number (Re), where inertial effects dominate. In contrast, viscous effects dominate the physics of low-Re fluid flows near small biological hairs. We anticipate rich nonlinear behaviour when deformable solids interact with fluid viscous effects[27–29]. Yet the reconfiguration problem of hair beds at low Re remains largely unsolved.

Here we investigate a bio-inspired model system of deformable hairs subject to low-Re fluid flows. Even though hairs and fluids are described by linear constitutive properties, we find the flow response of hair beds can exhibit two types of nonlinearities: a drag-reducing nonlinearity, which we characterize by the rescaled flow impedance $\widetilde{Z}$; and a rectification nonlinearity, which we find for angled hairs, and which we characterize by the impedance ratio Z_+/Z_- comparing flow with and against the grain. These two nonlinear responses are functions of the dimensionless parameter $\widetilde{\nu}$, which compares fluid and elastic effects.

Drag reduction

To investigate the feedback between hair deformation and fluid flow, we develop an experimental model system of elastomer hairs immersed in high-viscosity fluids (Fig. 1; Methods). We mount hair beds onto the inner rotor of a Taylor–Couette geometry (Supplementary Fig.1; Methods) and determine shear stress τ as a function of velocity v of the hairy surface. Upon first glance, rheometry experiments appear to exhibit shear thinning (Fig. 2a). For low velocities up to 0.01 m s^{-1}, shear stress τ scales linearly with v. But at higher velocities, τ deviates from linearity. We rule out shear thinning of the fluid because we observe nonlinearity at $\dot{\gamma} = (v/H - L) > 12.5\ \mathrm{s}^{-1}$, well below the fluid's known $\dot{\gamma}_{\mathrm{crit}} = 10{,}000\ \mathrm{s}^{-1}$. Instead, the measured nonlinear response arises from hair deformation.

To characterize this nonlinear behaviour, we develop a simple model to illustrate how fluid flow affects hair deformation. In Fig. 1d, we consider a stationary planar surface coated with hairs, immersed in fluid, and facing a smooth surface moving with velocity $v\mathbf{e}_x$ and separated by a distance H, measured from the hair base $z = 0$. No-slip boundary conditions hold at the moving surface. We further assume no-slip boundary conditions at the plane $z = h$ containing hair tips, which holds as long as the hair bed is sufficiently dense. The resulting flow profile $u(z) = v((z-h)/(H-h))$ is equivalent to the Couette problem of shear-driven flow between two plates—except that stresses from fluid flows cause hairs to bend (or reconfigure). As a result, the position of the hair-tip plane h depends on shear stress τ. At the same time, τ depends on h, because lowering the hair-tip plane increases the gap width $H - h$ and decreases the shear stress. This interdependency reflects the elastoviscous coupling between deformable hair beds and fluid flows.

[1]Hatsopoulos Microfluids Laboratory, Department of Mechanical Engineering, Massachusetts Institute of Technology, Cambridge, Massachusetts 02139, USA. [2]Hydrodynamics Laboratory, CNRS UMR 7646, Department of Mechanics, École Polytechnique, 91120 Palaiseau, France. *e-mail: peko@mit.edu

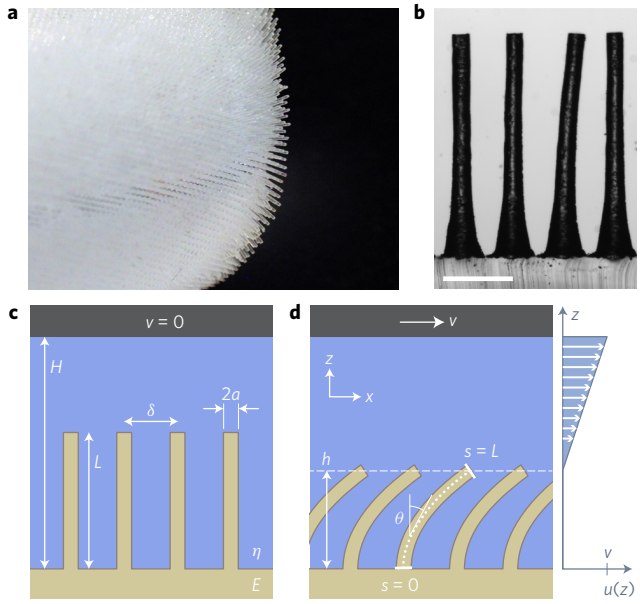

Figure 1 | Physical model of deformable hair beds coupled to low-Reynolds-number fluid flows. a, Photograph of dry elastomer hairs. **b**, Close-up micrograph of individual hairs. Scale bar, 1 mm. **c**, Schematic depicting seven relevant physical quantities: hair length L, hair diameter $2a$, hair separation δ (or equivalently, hair area packing fraction $\phi \cong a^2/\delta^2$), hair elastic modulus E, fluid viscosity η, channel height H, and wall velocity v. **d**, Schematic of hairs bending ('reconfiguration') in response to a finite plate velocity v. Hair backbone is characterized by backbone angle θ versus the curvilinear coordinate s. Hair height is given by h. Graph, right: Couette flow through a gap of width $H-h$.

We characterize the effect of elastoviscous coupling on the system's drag response by introducing the area-specific impedance Z (Fig. 2b), defined as:

$$Z(v) = \frac{\tau(v)}{v} = \frac{\eta}{H - h(v)} \tag{1}$$

Z relates the input velocity to the emergent shear stress of the system. It is related to the Stokes drag coefficient F_{drag}/v by a surface-area factor, where F_{drag} is the fluid force experienced by the hairy surface. If hairs are rigid, Z maintains a constant value Z_0 and $F_{\mathrm{drag}} \sim \tau \sim v$, as expected for linear Stokes flows (Fig. 2a,b; solid grey line). Meanwhile, if hairs deform, equation (1) shows that changes in the impedance will arise due to a purely geometrical contribution h, not from nonlinear viscous properties. As velocity increases, hairs bend towards the surface and Z approaches the value Z_∞ corresponding to a surface without hairs (Fig. 2a,b, dashed grey line).

To predict the form of Z as a function of v one must specify how hairs deform. By assuming hairs are packed sufficiently close together and deform identically, we consider a model of a single hair with shear stress concentrated at the tip. (We consider in the Supplementary Information a model where flow penetrates the hair-bed layer.) The curvilinear coordinate s follows the hair contour from base ($s=0$) to tip ($s=L$; Fig. 1d). The angle $\theta(s)$ of the backbone with respect to the surface normal characterizes the hair's shape. The position of the hair-tip plane is given by the functional $h[\theta(s)] = \int_0^L \cos(\theta(s))\,\mathrm{d}s$. Hairs are perpendicularly anchored at the base ($\theta|_{s=0} = 0$) and moment-free at the tip ($(\mathrm{d}/\mathrm{d}s)\theta|_{s=L} = 0$). In the limit where flow does not penetrate the bed layer, hairs deform elastically in response to a point force $\mathbf{F}$ resulting from the product of fluid shear stress τ and fibre area $\pi\delta^2 = (\pi a^2/\phi)$. The force $\mathbf{F} = (\pi a^2/\phi)\tau\mathbf{e}_x = (\pi a^2/\phi)(\eta v/(H-h))\mathbf{e}_x$ is applied at the hair tip. Note that the force is singular for $\phi \to 0$ or $h \to H$.

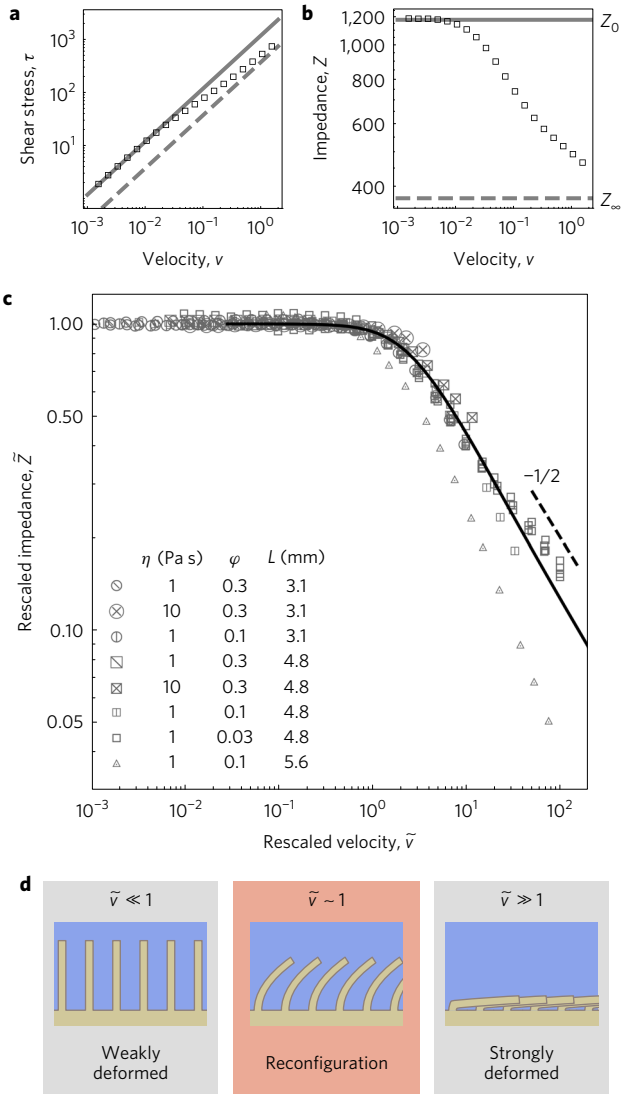

Figure 2 | Reconfiguration of beds of straight hairs. a, Shear stress τ (Pa) versus velocity v (m s^{-1}) of a cylinder coated with deformable, elastomer hairs subject to low-Re shear flows. Deviations from linearity show apparent shear-thinning behaviour. $\eta = 10^4$ cSt, $\phi = 0.227$. Grey solid line denotes the rigid-hair limit, dashed line the limit of a cylinder without hairs. **b**, Same results as **a**, but plotting area-specific impedance $Z = \tau/v$ (kg m^{-2} s^{-1}). Grey solid line denotes impedance Z_0 of weakly deformed hairs, dashed line Z_∞ of strongly deformed hairs. **c**, Rescaled impedance $\tilde{Z} = (Z - Z_\infty)/(Z_0 - Z_\infty)$ as a function of rescaled velocity $\tilde{v} = (4\eta L^2 v/E\phi a^2 H)(1-(L/H))^{-3/2}$. Experimental results (symbols), model (black solid line), and scaling behaviour at large $\tilde{v}$ (black dashed line) agree for hair beds of varying viscosity η, area packing fraction ϕ, and length L. **d**, Schematic of the three response regimes based on the rescaled velocity $\tilde{v}$.

The former limit, however, is not realized in our model because of the assumption that hairs are packed close together. The latter limit corresponds to the scenario where the hair tip comes in contact with the opposing surface. Force balance along $\mathbf{e}_z$ yields the following integro-differential equation of equilibrium:

$$0 = EI\frac{\mathrm{d}^2\theta(s)}{\mathrm{d}s^2} + \frac{\pi a^2}{\phi}\frac{\eta v\cos\theta(s)}{H - \int_0^L \cos\theta(s)\,\mathrm{d}s} \tag{2}$$

with $I = (\pi/4)a^4$ the second area moment of the hair's cross section. To gain physical insight, we make predictions of the form of the impedance when taking limiting values of the plate velocity v.

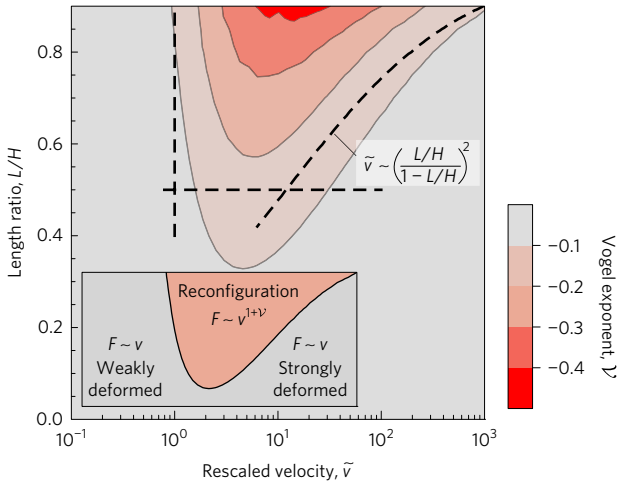

Figure 3 | The reconfiguration regime of straight hairs is characterized by a negative Vogel exponent. Numerically computed contour plot of the Vogel exponent $\mathcal{V}$ (given at low Re by $F \sim v^{1+\mathcal{V}}$) as a function of the length ratio L/H and rescaled velocity $\tilde{v} = (4\eta L^2 v/E\phi a^2 H)(1-(L/H))^{-3/2}$. Dashed lines correspond to the boundaries of the reconfiguration regime. Inset: schematic diagram of the reconfiguration regime (red), which is characterized by a significantly nonzero Vogel exponent, and thus anomalous scaling of force versus velocity. This behaviour contrasts the weakly and strongly deformed regimes (grey), where reconfiguration is negligible.

In the limit $v \to \infty$, hairs are strongly deformed as they bend towards the surface, and thus h tends towards zero (Fig. 2d, right). Because Z tends towards the constant Z_∞ in this limit, we instead determine the asymptotic behaviour of the quantity $\widetilde{Z} = (Z - Z_\infty)/(Z_0 - Z_\infty) = (h/H)((H-L)/(H-h))$, which we call rescaled impedance. In the strongly deformed limit $h \to 0$, we have for the rescaled impedance $\widetilde{Z} \sim h$: hair curvature is localized to a boundary layer of thickness h near the hair base. This scenario corresponds to the classical problem of a clamped rod pulled in an oblique direction and can be solved within the boundary layer (ref. 1, §4.4.1). The applied bending moment $F_{\mathrm{drag}} h \sim vh$ is balanced by EI/h (with curvature $\sim(1/h)$), yielding the prediction $\widetilde{Z} \sim v^{-1/2}$.

In the opposite limit $v \to 0$, hairs are only weakly deformed (Fig. 2d, left) and equation (2) can be solved in powers of v. Perturbation analysis to second order (Supplementary Information) yields a rescaled impedance $\widetilde{Z}$ that is predicted to depend on only one quantity, $\tilde{v} = (4\eta L^2 v/E\phi a^2 H)(1-(L/H))^{-3/2}$, which we call the rescaled velocity.

We compute $\widetilde{Z}$ and test the above predictions by numerically solving equation (2) (Methods). Indeed, we find $\widetilde{Z} \sim v^{-1/2}$ at high velocities (Fig. 2c, dashed line). We also find that $\widetilde{Z}$ can be well approximated by a function of $\tilde{v}$ alone (Supplementary Fig. 2). We further test the predictions of our model by performing shear rheology of immersed hair beds with varying L, ϕ, and η. Rescaling experimentally obtained $Z(v)$ measurements to $\widetilde{Z}(\tilde{v})$ collapses the data (Fig. 2c, symbols) onto a universal curve that agrees with our model (solid line). We observe that experimental data for the longest hairs (triangles) deviates from the model's prediction at high velocities. One possible reason for this disagreement may be that the elastomer hairs have a tapered, three-dimensional cylindrical shape, which contrasts the uniform, one-dimensional contours in our model. Although we do account for tapered contours (Supplementary Information), the hairs' behaviour at large deformation is probably sensitive to their actual shape.

The rescaled velocity $\tilde{v}$ is a dimensionless parameter that controls the response of hair beds (Fig. 2d). The value $\tilde{v} = 1$ separates the weakly deformed and strongly deformed limits (Table 1). The rescaled velocity comprises two dimensionless groups ($4\eta L^2 v/E\phi a^2 H$) and L/H, each of which have a physical interpretation. The dimensionless group ($4\eta L^2 v/E\phi a^2 H$) is an elastoviscous parameter that compares fluid and elastic effects, and bears some resemblance to elastoviscous parameters in other studies[30–32]. There is a roughly one-to-one correspondence between the value of this group and hair contour shape (Supplementary Fig. 3). Indeed, hairs bend more when increasing η, L, or v; or when decreasing E, ϕ, a, or H. Meanwhile, the ratio L/H of hair length to channel width expresses the effect of confinement on $\widetilde{Z}$. The length ratio L/H is related to the impedance ratio $(Z_0/Z_\infty) = 1/(1-L/H)$ between undeformed and fully deformed hairs.

The rescaled impedance $\widetilde{Z}$ is a function of one variable: the rescaled velocity $\tilde{v}$. However, the (dimensional) impedance Z includes an additional dependence on the length ratio L/H:

$$\frac{Z}{Z_\infty} = \widetilde{Z}\frac{L/H}{1-L/H} + 1 \qquad (3)$$

The longer the hairs ($L \to H$), the stronger the effect of reconfiguration (expressed by $\widetilde{Z}$) on Z. Conversely, if the opposing surface is far away ($H \to \infty$), impedance tends to $Z_\infty \to 0$. The latter limiting scenario, which is reminiscent of Stokes' paradox[33], highlights the importance of confinement due to the channel width H in this low-Re problem[32].

Several studies have investigated the deformation of flexible solid objects subject to high-Re flows. These studies have established that deformation typically leads to a reduction of the drag coefficient[14–19,21–24,26] (although increases have also been measured[22]). Changes in the drag coefficient lead to anomalous scaling $F_{\mathrm{drag}} \sim v^{2+\mathcal{V}}$, where the so-called Vogel exponent $\mathcal{V}$ captures the effect of reconfiguration on drag response.

Here we define the Vogel exponent at low Re by the relation $F_{\mathrm{drag}} \sim v^{1+\mathcal{V}}$, or equivalently, $Z \sim v^{\mathcal{V}}$ and thus $\mathcal{V} = (\mathrm{d}\log Z/Z_\infty)/(\mathrm{d}\log\tilde{v})$. In the two opposing limits of undeformed and fully deformed hairs, both of which have constant impedance, $\mathcal{V}$ vanishes. Significantly nonzero Vogel exponents occur only in a crossover region around $\tilde{v} \sim 1$, which we call the reconfiguration regime (Fig. 3). Within the reconfiguration regime, the Vogel exponent $\mathcal{V}$ attains negative values (Fig. 3, red areas). Negative $\mathcal{V}$ corresponds to apparent shear-thinning behaviour, or equivalently, drag reduction. The boundaries of the reconfiguration regime are given by the following arguments. $L/H \gtrsim 1/2$ holds, otherwise the constant term in equation (3) dominates. The weakly deformed assumption breaks down when $\tilde{v}$ exceeds one. The strongly deformed regime begins when the left-hand term in $\widetilde{Z}$ of equation (3) is much less than one, yielding $v^{1/2} \gg (L/H)/(1-L/H)$. Although the value of $\mathcal{V}$ varies within the reconfiguration regime, equation (3) produces $\mathcal{V} \to -1/2$ when $L \to 1$ inside the reconfiguration regime. A numerical computation of $\mathcal{V}$ agrees with this limiting value and the boundaries of the reconfiguration regime (Fig. 3, dashed lines). The value $-1/2$ of the Vogel exponent in our low-Re problem stands in contrast to the values of $-2/3$ to $-4/3$ found in reconfiguration studies at high Re[21,22,24,26]. The lower Vogel exponent we find at low Re may indicate a more limited contribution of reconfiguration to the system's flow response compared to the high-Re case.

Rectification

So far we have considered hairs that are anchored perpendicularly to the surface, with anchoring angle $\theta_0 = 0$ (Fig. 4a). This configuration is invariant to reflections across certain symmetry planes normal to the surface. Angled hairs, which are anchored subnormally to the surface with finite θ_0, break reflection symmetry (Fig. 4b). Does the asymmetry in geometry yield an asymmetric drag response? At high Re, changing the sign of v affects vortex shedding and thus drag

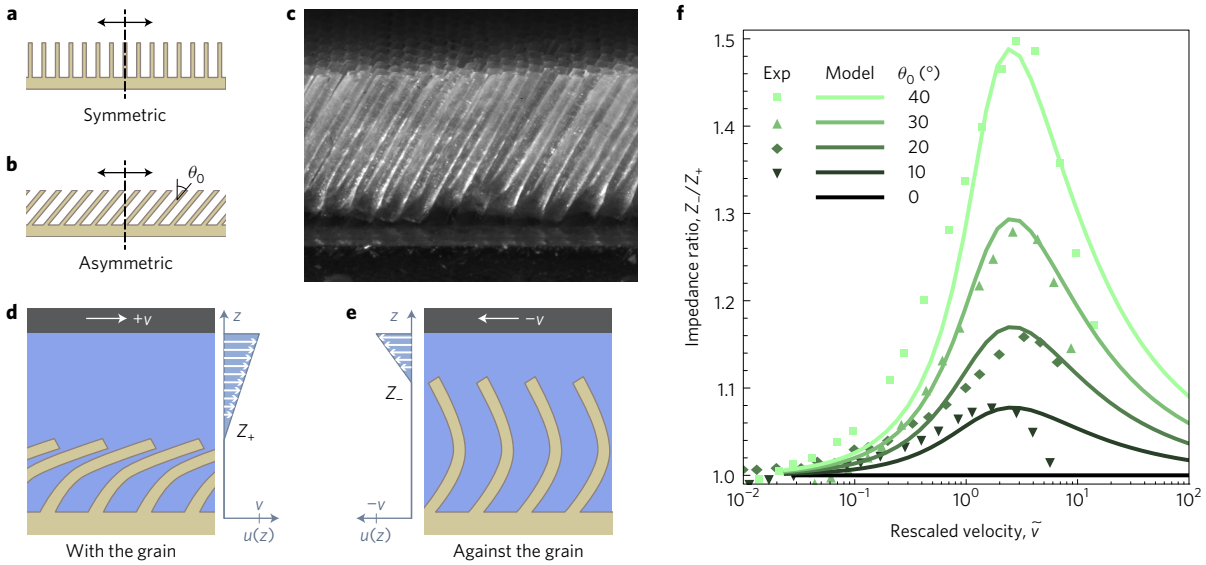

Figure 4 | Angled hairs break reflection symmetry, both in geometry as well as in drag response. a, Schematic of straight hairs, cantilevered perpendicularly to the base. This configuration is invariant to reflections about hair axes (dashed line). **b**, Schematic of hairs anchored at an angle θ_0 with respect to the surface normal, which break reflection symmetry. **c**, Photograph of elastomer hairs with $\theta_0 = 30°$. **d**, Schematic of angled hairs bending down in response to flow with the grain. **e**, For flow against the grain, hairs bend up and decrease the gap through which fluid flows. This results in an impedance (Z_-) that is larger than for flow with the grain (Z_+). **f**, Impedance ratio Z_-/Z_+ as a function of the rescaled velocity $\tilde{v} = (4\eta L^2 v/E\phi a^2 H)(1-(L/H)\cos\theta_0)^{-3/2}$. Larger values of Z_-/Z_+ correspond to increased rectification. Experimental results (symbols) and numerical results (lines) for hair beds of different anchoring angles θ_0 (legend, top left). Hair dimensions satisfy $L\cos\theta_0/H = 0.47$.

Table 1 | Scaling of dynamical quantities.

Weakly deformed	Reconfiguration	Strongly deformed
$\tilde{Z} \sim v^0$	Crossover	$\tilde{Z} \sim v^{-1/2}$
$Z \sim v^0$	$Z \sim v^{\mathcal{V}}$	$Z \sim v^0$
$F_{drag} \sim v^1$	$F_{drag} \sim v^{1+\mathcal{V}}$	$F_{drag} \sim v^1$
$Z_-/Z_+ \to 1$	$Z_-/Z_+ \geq 1$	$Z_-/Z_+ \to 1$

response. At low Re, the reversibility of Stokes' equation dictates that changing the sign of v would leave Z unaffected—provided hairs are rigid. It is well known in the context of swimmers at low Re that flexibility introduces nonlinearities that can break Stokes' symmetry and allow forward locomotion[34]. However, it remains unclear under which conditions, and to what degree, flexibility results in an asymmetric drag response in the context of hair beds. In the following, we show that hair beds with a nonzero anchoring angle θ_0 give rise to an axially asymmetric drag response in the reconfiguration regime.

To this end, we replace the first boundary condition of equation (2) with $\theta|_{s=0} = \theta_0$. As a result, the quantity θ_0 appears in the impedances Z_0, $\tilde{Z}$, and Z/Z_∞, as well as the rescaled velocity $\tilde{v}$ (Methods). We again solve numerically for impedance. We also modify our manufacturing process to produce hair beds with a nonzero anchoring angle θ_0 up to 40° (Methods; Fig. 4c). Different behaviour emerges depending on the sign of the velocity.

When fluid flows in the same direction as hair tilt (flow with the grain), hairs bend down towards the base. This scenario is similar to the case of reconfiguration of straight hairs. (Fig. 4d and Supplementary Fig. 4). As a result, varying θ_0 does not significantly change the form of $\tilde{Z}$ (Supplementary Fig. 5), and the Vogel exponent remains negative (Fig. 5a).

When flow opposes hair tilt (flow against the grain), hairs initially bend up away from the base (Fig. 4e). Upward bending increases hair height h and decreases the gap width $H-h$. The narrowing gap implies that impedance against the grain (Z_-) is greater compared to flow with the grain (Z_+). This results in positive values of the Vogel exponent (Fig. 5b). This behaviour occurs until hair height and impedance approach a maximum, which occurs near $\tilde{v} \approx 1$. Further increasing flow velocity causes hairs to bend back towards the base, and negative Vogel exponents are again recovered. This behaviour is qualitatively similar to high-Re results in ref. 22.

We express directionality of drag response with the ratio Z_-/Z_+ (Fig. 4f) of impedances against and with the grain, respectively. This ratio is identical to one for straight hairs ($\theta_0 = 0$). For angled hairs in the weakly and strongly deformed limits, Z_-/Z_+ is approximately equal to one. Only for angled hairs in the reconfiguration regime does Z_-/Z_+ exhibit a peak centred near $\tilde{v} \approx 1$. The maximum value of this peak depends on L/H and θ_0 (Supplementary Fig. 4b). We find reasonable agreement between experimental (symbols) and numerically computed (lines) values of Z_-/Z_+. However, at high velocity, we find that experimental values deviate from our model's prediction. One possible reason for this disagreement may again be the tapered, three-dimensional cylindrical shape of hairs, whose behaviour at large deformation is not captured by our simple model.

In our experiments, we attained a maximal peak value of $Z_-/Z_+ \approx 1.5$ with $L/H = 0.62$ and $\theta_0 = 40°$. Improved rectification could be attained by increasing hair length L or anchoring angle θ_0. It is interesting to note that our simple model encounters a singularity as $h \to H$, where Z_-/Z_+ would become arbitrarily large. In reality, one must consider penetration of flow into the hair bed, which removes this singularity (Supplementary Information).

Discussion

To summarize, we have shown that beds of deformable hairs can reconfigure in response to fluid flows. We identified a dimensionless, elastoviscous parameter $\tilde{v}$, which defines different response regimes. When $\tilde{v}$ is of order one, hair reconfiguration results in a nonlinear response. When hairs are straight, or when fluid flows with the grain of angled hairs, we find a drag-reducing nonlinear response, characterized by a negative Vogel exponent $\mathcal{V}$. In contrast, drag-increasing response and positive $\mathcal{V}$ occur when fluid flows against the grain of angled hairs. We were able to

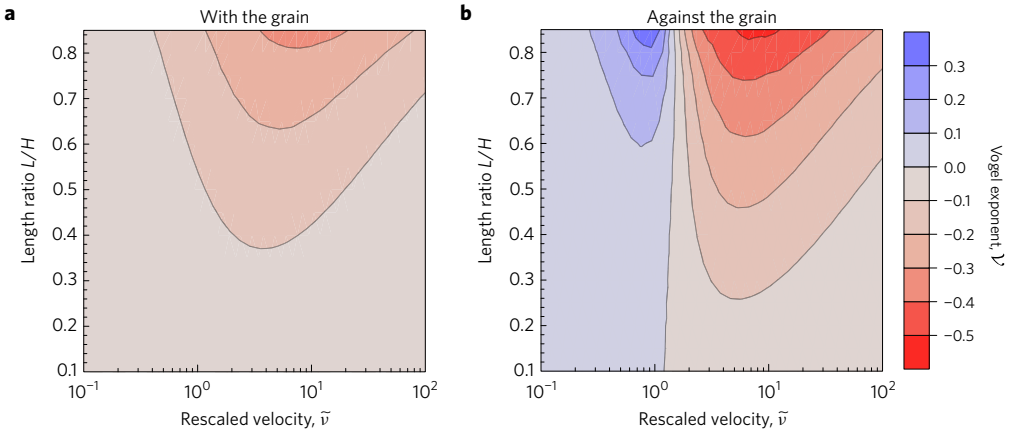

Figure 5 | The reconfiguration regime of angled hairs is characterized by a Vogel exponent that can attain positive values when flow is against the grain. a, Numerically computed contour plot of the Vogel exponent $\mathcal{V}$ as a function of the length ratio L/H and rescaled velocity $\tilde{v}=(4\eta L^2 v/E\phi a^2 H)(1-(L/H)\cos\theta_0)^{-3/2}$ for hairs with $\theta_0=30°$ and flow with the grain. **b**, $\mathcal{V}$ for flow against the grain. Blue areas denote a positive Vogel exponent.

probe these nonlinear responses by assuming that shear stress is concentrated at the hair tip. This simplifying assumption dispenses with the need to integrate stresses over the entire hair surface, and allows us to probe beyond the linear regime[35].

The drag-reducing response of straight hairs, which we described with the rescaled impedance $\tilde{Z}$ (see Fig. 2c), provides experimental evidence that hairy surfaces reconfigure to reduce the shear stress experienced by the anchoring surface. Hair beds such as the hyaluronan brushes of blood vessels[11,13] or brush-border microvilli of kidney tubules[7] have been implicated in mechanotransduction, in analogy to experimental systems where hair deflection is used to sense fluid forces[36–41]. Our work raises the hypothesis that the drag-reducing nonlinearity of biological hair beds protects sensitive mechanotransductive mechanisms from excessive stresses.

Additionally, the drag-reducing and drag-increasing response of angled hairs amounts to rectification, or an axially asymmetric flow response, which we express by the impedance ratio Z_-/Z_+ (see Fig. 4f). Prior studies have shown that control over a rectification response can lead to the development of diverse microfluidic components, such as pumps and diodes[42–44]. Typically, rectification at low Re is challenging to attain because the governing Stokes equations are linear and time-reversible. Existing designs have overcome this difficulty by employing viscoelastic fluids[42] or anisotropic surface-wetting properties[43,44]. The rectification response we report here instead relies on a geometric nonlinearity, whose operating range can be controlled by the geometric factors embedded in $\tilde{v}$. The rectification nonlinearity of angled hairs holds at arbitrarily low Reynolds number and is compatible with Newtonian fluids and conventional surfaces. Future work could lead to the design of integrated microfluidic components such as diodes and pumps.

Methods

Methods, including statements of data availability and any associated accession codes and references, are available in the online version of this paper.

Received 3 February 2017; accepted 4 July 2017; published online 21 August 2017

References

1. Audoly, B. & Pomeau, Y. *Elasticity and Geometry: From Hair Curls to the Non-linear Response of Shells* (Oxford Univ. Press, 2010).
2. Vogel, S. & Davis, K. K. *Cats' Paws and Catapults: Mechanical Worlds of Nature and People* (Norton, 2000).
3. Stoop, N., Lagrange, R., Terwagne, D., Reis, P. M. & Dunkel, J. Curvature-induced symmetry breaking determines elastic surface patterns. *Nat. Mater.* **14,** 337–342 (2015).
4. Krishnamurthy, D., Katsikis, G., Bhargava, A. & Prakash, M. *Schistosoma mansoni* cercariae swim efficiently by exploiting an elastohydrodynamic coupling. *Nat. Phys.* **13,** 266–271 (2016).
5. Wehner, M. *et al*. An integrated design and fabrication strategy for entirely soft, autonomous robots. *Nature* **536,** 451–455 (2016).
6. Kwak, M. K., Jeong, H.-E., Kim, T.-i., Yoon, H. & Suh, K. Y. Bio-inspired slanted polymer nanohairs for anisotropic wetting and directional dry adhesion. *Soft Matter* **6,** 1849–1857 (2010).
7. Guo, P., Weinstein, A. M. & Weinbaum, S. A hydrodynamic mechanosensory hypothesis for brush border microvilli. *Am. J. Physiol.* **279,** F698–F712 (2000).
8. Harper, C. J., Swartz, S. M. & Brainerd, E. L. Specialized bat tongue is a hemodynamic nectar mop. *Proc. Natl Acad. Sci. USA* **110,** 8852–8857 (2013).
9. Schwartz, E. A., Leonard, M. L., Bizios, R. & Bowser, S. S. Analysis and modeling of the primary cilium bending response to fluid shear. *Am. J. Physiol.* **272,** F132–F138 (1997).
10. Young, Y. N., Downs, M. & Jacobs, C. R. Dynamics of the primary cilium in shear flow. *Biophys. J.* **103,** 629–639 (2012).
11. Weinbaum, S., Zhang, X., Han, Y., Vink, H. & Cowin, S. C. Mechanotransduction and flow across the endothelial glycocalyx. *Proc. Natl Acad. Sci. USA* **100,** 7988–7995 (2003).
12. Weinbaum, S., Tarbell, J. M. & Damiano, E. R. The structure and function of the endothelial glycocalyx layer. *Annu. Rev. Biomed. Eng.* **9,** 121–167 (2007).
13. VanTeeffelen, J. W., Brands, J., Stroes, E. S. & Vink, H. Endothelial glycocalyx: sweet shield of blood vessels. *Trends Cardiovasc. Med.* **17,** 101–105 (2007).
14. Vogel, S. Drag and reconfiguration of broad leaves in high winds. *J. Exp. Bot.* **40,** 941–948 (1989).
15. Luhar, M. & Nepf, H. M. Flow-induced reconfiguration of buoyant and flexible aquatic vegetation. *Limnol. Oceanogr.* **56,** 2003–2017 (2011).
16. Albayrak, I., Nikora, V., Miler, O. & O'Hare, M. T. Flow–plant interactions at leaf, stem and shoot scales: drag, turbulence, and biomechanics. *Aquat. Sci.* **76,** 269–294 (2013).
17. Vollsinger, S., Mitchell, S. J., Byrne, K. E., Novak, M. D. & Rudnicki, M. Wind tunnel measurements of crown streamlining and drag relationships for several hardwood species. *Can. J. For. Res.* **35,** 1238–1249 (2005).
18. Alben, S., Shelley, M. & Zhang, J. Drag reduction through self-similar bending of a flexible body. *Nature* **420,** 479–481 (2002).
19. Favier, J., Dauptain, A., Basso, D. & Bottaro, A. Passive separation control using a self-adaptive hairy coating. *J. Fluid Mech.* **627,** 451–483 (2009).
20. Battiato, I., Bandaru, P. R. & Tartakovsky, D. M. Elastic response of carbon nanotube forests to aerodynamic stresses. *Phys. Rev. Lett.* **105,** 144504 (2010).
21. Gosselin, F., De Langre, E. & Machado-Almeida, B. Drag reduction of flexible plates by reconfiguration. *J. Fluid Mech.* **650,** 319–341 (2010).
22. Gosselin, F. P. & de Langre, E. Drag reduction by reconfiguration of a poroelastic system. *J. Fluids Struct.* **27,** 1111–1123 (2011).
23. Brücker, C. *Progress in Turbulence and Wind Energy IV* 191–196 (Springer, 2012).
24. de Langre, E., Gutierrez, A. & Cossé, J. On the scaling of drag reduction by reconfiguration in plants. *C. R. Méc.* **340,** 35–40 (2012).

25. Schouveiler, L. & Eloy, C. Flow-induced draping. *Phys. Rev. Lett.* **111,** 064301 (2013).
26. Leclercq, T. & de Langre, E. Drag reduction by elastic reconfiguration of non-uniform beams in non-uniform flows. *J. Fluids Struct.* **60,** 114–129 (2016).
27. Duprat, C., Protière, S., Beebe, A. Y. & Stone, H. A. Wetting of flexible fibre arrays. *Nature* **482,** 510–513 (2012).
28. Saintyves, B., Jules, T., Salez, T. & Mahadevan, L. Self-sustained lift and low friction via soft lubrication. *Proc. Natl Acad. Sci. USA* **113,** 5847–5849 (2016).
29. *Fluid-Structure Interactions in Low-Reynolds-Number Flows* (eds Duprat, C. & Stone, H.) (RSC Soft Matter Series, The Royal Society of Chemistry, 2016).
30. Trouilloud, R., Yu, T. S., Hosoi, A. E. & Lauga, E. Soft swimming: exploiting deformable interfaces for low Reynolds number locomotion. *Phys. Rev. Lett.* **101,** 048102 (2008).
31. Coq, N., du Roure, O., Marthelot, J., Bartolo, D. & Fermigier, M. Rotational dynamics of a soft filament: wrapping transition and propulsive forces. *Phys. Fluids* **20,** 051703 (2008).
32. Wexler, J. S. *et al*. Bending of elastic fibres in viscous flows: the influence of confinement. *J. Fluid Mech.* **720,** 517–544 (2013).
33. Kundu, P. K., Cohen, I. M. & Dowling, D. R. *Fluid Mechanics* (Elsevier Science, 2015).
34. Purcell, E. M. Life at low Reynolds number. *Am. J. Phys.* **45,** 3–11 (1977).
35. Gopinath, A. & Mahadevan, L. Elastohydrodynamics of wet bristles, carpets and brushes. *Proc. R. Soc. A* **467,** 1665–1685 (2011).
36. Brücker, C., Spatz, J. & Schröder, W. Feasability study of wall shear stress imaging using microstructured surfaces with flexible micropillars. *Exp. Fluids* **39,** 464–474 (2005).
37. Große, S., Schröder, W. & Brücker, C. Nano-newton drag sensor based on flexible micro-pillars. *Meas. Sci. Technol.* **17,** 2689–2697 (2006).
38. Brücker, C., Bauer, D. & Chaves, H. Dynamic response of micro-pillar sensors measuring fluctuating wall-shear-stress. *Exp. Fluids* **42,** 737–749 (2007).
39. Brücker, C. Interaction of flexible surface hairs with near-wall turbulence. *J. Phys. Condens. Matter* **23,** 184120 (2011).
40. Paek, J. & Kim, J. Microsphere-assisted fabrication of high aspect-ratio elastomeric micropillars and waveguides. *Nat. Commun.* **5,** 3324 (2014).
41. Brücker, C. Evidence of rare backflow and skin-friction critical points in near-wall turbulence using micropillar imaging. *Phys. Fluids* **27,** 031705 (2015).
42. Groisman, A. & Quake, S. A microfluidic rectifier: anisotropic flow resistance at low Reynolds numbers. *Phys. Rev. Lett.* **92,** 094501 (2004).
43. Mates, J. E., Schutzius, T. M., Qin, J., Waldroup, D. E. & Megaridis, C. M. The fluid diode: tunable unidirectional flow through porous substrates. *ACS Appl. Mater. Interfaces* **6,** 12837–12843 (2014).
44. Li, L., Mo, J. & Li, Z. Nanofluidic diode for simple fluids without moving parts. *Phys. Rev. Lett.* **115,** 134503–134505 (2015).

Acknowledgements

We thank A. Nasto, A. Helal, A. Gopinath, K. Hood and B. Keshavarz for insightful discussions; K. Broderick for fabrication assistance; F. Frankel for photography of hairs; and S. Lin for tensiometry experiment. A.E.H. acknowledges support from the Defense Advanced Research Projects Agency and US Army Research Office under grant numbers DARPA W31P4Q-13-1-0013 and ARO W911NF-15-1-0166. J.A. acknowledges support the US Army Research Office under grant number W911NF-14-1-0396.

Author contributions

J.A., J.C. and A.E.H. conceived the project. J.A. performed experiments. J.A., J.C. and E.d.L. contributed to theoretical models. All authors contributed to the paper.

Additional information

Supplementary information is available in the online version of the paper. Reprints and permissions information is available online at www.nature.com/reprints. Publisher's note: Springer Nature remains neutral with regard to jurisdictional claims in published maps and institutional affiliations. Correspondence and requests for materials should be addressed to A.E.H.

Competing financial interests

The authors declare no competing financial interests.

Methods

Hair beds. Hair beds are fabricated based on a previously published protocol[45]. In short, we cut a hexagonal array of holes in a clear acrylic sheet using a laser cutter (VersaLaser, Universal Laser Systems) and cast with polydimethylsiloxane elastomer (Dow Corning; $E = 2$ MPa). Hairs have length $L = 3.1$–5.6 mm, diameter $2a \approx 0.29$ mm, and hair separation $\delta = 0.50$–1.38 mm (resulting in area packing fraction $\phi = (2\pi/\sqrt{3})(a^2/\delta^2) \approx 0.03$–$0.3$). Hairs have a tapered thickness profile, which we measure to compute effective diameters and lengths (Supplementary Information). Hair beds are mounted onto the inner cylinder of a Taylor–Couette geometry (inner radius $R_i = 15$ mm, outer radius $R_o = 22$ mm, length $L_{cyl} = 42.2$ mm; $N \sim 10^4$ hairs) and immersed in silicone oil (Gelest, viscosity $\eta = 10^3$–10^4 cPs, density $\rho = 970\,\mathrm{kg\,m^{-3}}$). For angled hairs, we custom-built supports that hold the acrylic stock at an angle while laser cutting.

Rheometry. We measure torque T as a function of rotational velocity ω using a magnetic-bearing rheometer (AR-G2, TA Instruments). We then determine shear stress $\tau = (T/2\pi L_{cyl} R_{base}^2)$ and velocity $v = R_{base}\omega$, where R_{base} is the radius of the base of the hairs. The impedance of undeformed hairs Z_0 is determined by computing the mean of Z in a plateau around $\widetilde{v} \approx 10^{-1}$, and $Z_\infty = c((R_{out}^2 - R_{tip}^2)/(R_{out}^2 - R_{base}^2))Z_0$, where R_{out} is the inner radius of the outer cylinder and R_{tip} is the radius of the tip of undeformed hairs, and $c = 0.7$ a fit parameter. All radii are taken with respect to the cylindrical axis of the rheometer. Velocities $v = \omega R_i$ correspond to Reynolds number $\mathrm{Re} = \rho v H/\eta = 0.001$–$2$. For Fig. 2c, rescaled velocity $v = k(4\eta L^2 v/E\phi a^2 H)(1 - L/H)^{-3/2}$, with $k = 2$ a fit parameter, is computed by using effective values of L and a (Supplementary Information).

Numerics. We numerically solve equation (2) with Mathematica (v. 11.0). We first guess a constant value for the initial hair height $h_1 = L$. Next, we solve for $\theta(s)$ using the 'NDSolve' function of Mathematica ('Shooting' method, starting from an undeformed hair tip). We then compute h_2 with the resulting solution, which is used as a guess for the next iteration. We perform iterations until $h_i - h_{i-1}$ converges to the third decimal.

Impedance for angled hairs. Introducing the parameter θ_0 introduces extra trigonometric factors in the following impedance definitions:

$$Z_0 = \frac{\eta}{H - L\cos\theta_0}$$

$$\widetilde{Z} = \frac{h}{L\cos\theta_0}\,\frac{H - L\cos\theta_0}{H - h}$$

$$\frac{Z}{Z_\infty} = \widetilde{Z}\left(\frac{L\cos\theta_0}{H - L\cos\theta_0}\right) + 1$$

$$\widetilde{v} = \frac{4\eta L^2 v}{E\phi a^2 H}\left(1 - \frac{L\cos\theta_0}{H}\right)^{-3/2}$$

Data availability. The data that support the plots within this paper and other findings of this study are available from the corresponding author upon request.

References

45. Nasto, A. *et al*. Air entrainment in hairy surfaces. *Phys. Rev. Fluids* **1,** 033905 (2016).